High Energy Density Physics 9 (2013) 583–593

Contents lists available at SciVerse ScienceDirect

High Energy Density Physics

journal homepage: www.elsevier.com/locate/hedp

Versatile code DLAYZ for investigating population kinetics and radiative properties of plasmas in non-local thermodynamic equilibrium

Cheng Gao [a], Jiaolong Zeng [a,*], Yongqiang Li [a], Fengtao Jin [a], Jianmin Yuan [a,b,*]

[a] Department of Physics, College of Science, National University of Defense Technology, Changsha 410073, Hunan, PR China
[b] State Key Laboratory of High Performance Computing, National University of Defense Technology, Changsha 410073, Hunan, PR China

ARTICLE INFO

Article history:
Received 27 May 2013
Accepted 27 May 2013
Available online 5 June 2013

Keywords:
Non-local thermodynamic equilibrium
Population kinetics
Radiative property

ABSTRACT

A versatile code DLAYZ based on collisional-radiative model is developed for investigating the population kinetics and radiative properties of plasmas in non-local thermodynamic equilibrium. DLAYZ is implemented on the detailed level accounting (DLA) approach and can be extended to detailed configuration accounting (DCA) and hybrid DLA/DCA approaches. The code can treat both steady state and time-dependent problems. The implementation of the main modules of DLAYZ is discussed in detail including atomic data, rates, population distributions and radiative properties modules. The complete set of basic atomic data is obtained using relativistic quantum mechanics. For dense plasmas, the basic atomic data with plasma screening effects can be obtained. The populations are obtained by solving the coupled rate equations, which are used to calculate the radiative properties. A parallelized version is implemented in the code to treat the large-scale rate equations. Two illustrative examples of a steady state case for carbon plasmas and a time-dependent case for the relaxation of a K-shell excited argon are employed to show the main features of the present code.

1. Introduction

Population kinetics and radiative properties of plasmas are and will remain a subject of interest since they have important applications in research fields such as inertial confinement fusion (ICF) and stellar physics [1–3]. In indirect driven ICF experiments, for example, the inside wall of a hohlraum, usually made of gold, is irradiated by high power lasers and the gold plasma produced emits strong X-ray radiation to drive the target implosion. In order to understand the physics of, e.g., energy deposition and temperature relaxation and to optimize the design of the hohlraum and target, knowledge of the population kinetics and radiative properties of gold plasmas is essential.

For plasmas in local thermodynamic equilibrium (LTE), populations can be obtained by solving Saha–Boltzmann equation and then the radiative properties of plasmas can be calculated [4–7]. However, in many circumstances plasmas are in non-LTE (NLTE) and much effort has been devoted to population distributions and radiative properties of NLTE plasmas recently (see the articles of NLTE code comparison workshops reported in Ref. [8]). Theoretically, collisional-radiative (CR) models were widely used to obtain the population distributions in NLTE plasmas by solving the coupled rate equations for the atomic states. These CR models were developed based on various approaches such as detailed-configuration-accounting (DCA) [9–11], average atom (AA) [12–16] and the super-configuration approach (SCA) [17–19]. In order to obtain the population distributions and radiative properties of NLTE plasmas rapidly, calculational methods were also developed by using atomic data obtained analytically in CR models [20–23]. Large discrepancies are found between different theoretical models due primarily to the different accuracy of atomic data [8]. Normally, the detailed-level-accounting (DLA) approach is considered one of the most accurate methods which explicitly includes the information of fine structure levels [24–28]. The DLA method, however, is usually used for low-Z plasmas [29] and a large computational effort is needed for high-Z plasmas [30]. To balance the computational accuracy and cost for complex systems, hybrid models combining detailed and statistical methods have been developed [31]. Due to the complexity of the problem, large discrepancies were found between results obtained by different codes [8]. To

* Corresponding authors. Department of Physics, College of Science, National University of Defense Technology, Changsha 410073, Hunan, PR China.
E-mail addresses: jiaolongzeng@hotmail.com (J. Zeng), jmyuan@nudt.edu.cn (J. Yuan).

1574-1818/$ – see front matter © 2013 Elsevier B.V. All rights reserved.
http://dx.doi.org/10.1016/j.hedp.2013.05.014

elucidate the origin of these discrepancies, accurate theoretical models are needed.

We present a detailed description of our NLTE model named DLAYZ for the investigation of population kinetics and radiative properties of plasmas. The code was first developed based on a DLA approach, which contains a complete set of atomic data between fine structure levels by using a fully relativistic quantum mechanical method. More recently DLAYZ was extended to DCA and hybrid DLA/DCA approaches. A parallelized version has been developed to solve the rate equations with level numbers larger than 10^4. DLAYZ can treat the steady state and time-dependent NLTE problems. These features make it a versatile NLTE code for investigating the population kinetics and radiative properties from low-Z to high-Z plasmas. This paper is organized as follows. In Section 2, the present model is described, where the modules of DLAYZ are introduced. In Section 3, two examples are illustrated containing a steady state case and a time-dependent case. A conclusion is given in Section 4.

2. Model description

The objective of DLAYZ code is to compute atomic level populations and radiative properties of NLTE plasmas over a broad range of plasma conditions, by using the DLA formalism. Additionally, it can easily be extended to DCA and hybrid DLA/DCA approximation. In the following, we give a complete description on the different aspects of the DLA formalism, which is accurate to fine-structure levels of plasma ions. For a CR model, the essential components include a description of the atomic levels and the processes that couple these levels. Detailed information of the population of any ion in a given level can be obtained by solving the coupled rate equations, which is constructed with a choice of levels and the microscopic atomic processes that coupled the levels. Once the plasma ionization balance is determined, the radiative properties such as opacity and emissivity can be derived.

In the CR model, the population n_i of fine-structure level i is obtained by solving the rate equation

$$\frac{\mathrm{d}n_i}{\mathrm{d}t} = \sum_{j\neq i}^{N_\mathrm{L}} n_j R_{ji} - n_i \sum_{j\neq i}^{N_\mathrm{L}} R_{ij}, \tag{1}$$

where N_L is the total number of levels included in the rate equation, R_{ji} and R_{ij} are the total populating and depopulating rates for the level i due to different atomic processes, including photo-excitation and ionization, electron impact excitation and ionization, Auger decay and their reverse processes. To solve this equation, we need the rates as the input, which are determined by the basic atomic data including various cross sections for the interaction of photons and electrons with the ions.

2.1. Atomic data module

The computation of various atomic radiative and collisional processes involves the bound and continuum states of different successive ionization stages in the plasmas. For the bound states, a fully relativistic approach based on the Dirac equation is used while for the continuum processes the distorted wave approximation is employed [28,32].

The bound states of the atomic system are calculated in the configuration interaction approximation. The radial orbitals for the construction of basis states are derived from a modified self-consistent Dirac–Fock–Slater iteration on a fictitious mean configuration with fractional occupation numbers, representing the average electron cloud of the configurations included in the calculation. Explicitly, the atomic structure is determined by diagonalizing the relativistic Hamiltonian [32]:

$$H = \sum_{i=1}^{N} H_\mathrm{D}(i) + \sum_{i<j}^{N} \frac{1}{r_{ij}}, \tag{2}$$

where $H_\mathrm{D}(i)$ is the single-electron Dirac Hamiltonian and N is the number of bound electrons. The basis states ϕ_j, which are referred to as configuration state functions (CSF), are antisymmetric sums of the products of N one-electron Dirac spinors $\varphi_{n\kappa m}$

$$\varphi_{n\kappa m} = \frac{1}{r}\begin{pmatrix} P_{n\kappa}(r)\chi_{\kappa m}(\theta,\psi,\sigma) \\ iQ_{n\kappa}(r)\chi_{-\kappa m}(\theta,\psi,\sigma) \end{pmatrix}, \tag{3}$$

where $P_{n\kappa}(r)$ and $Q_{n\kappa}(r)$ are radial functions for the large and small components of the orbital, $\chi_{\kappa m}(\theta,\psi,\sigma)$ is a two-component spherical spinor, n, κ and m are the principal, relativistic angular, and magnetic quantum number, respectively. The relativistic angular quantum number κ is linked with non-relativistic (l) and total (j) angular quantum number by $\kappa = (l-j)(2j+1)$. The large and small components, $P_{n\kappa}(r)$ and $Q_{n\kappa}(r)$, satisfy the coupled Dirac equation for a local central field in the standard Dirac–Fock–Slater method. The local central potential includes the contributions from the nuclear charge and the electron–electron interaction. The standard jj coupling scheme is used in coupling the angular momenta of successive shells. Various orbitals are assumed to be orthonormal:

$$\int_0^\infty (P_{n\kappa}P_{n'\kappa} + Q_{n\kappa}Q_{n'\kappa})\mathrm{d}r = \delta_{nn'}. \tag{4}$$

An atomic state function is approximated by a linear combination of CSFs with the same symmetry

$$\Psi(J\pi) = \sum_{j=1}^{n_\mathrm{c}} a_j \phi_j(J\pi), \tag{5}$$

where n_c is the number of CSFs and a_j denotes the representation of the atomic state in this basis.

After obtaining the wavefunctions, we can calculate the required atomic data to construct the rate equations. For a radiative transition from level i to j, the rate is given by

$$A_{ij} = 2\frac{(\alpha\Delta E)^{2L+1}}{g_i(2L+1)}\left|\left\langle \Psi_j \parallel O_M^L \parallel \Psi_i \right\rangle\right|^2 \tag{6}$$

where Ψ_i and Ψ_j are atomic wave function of level i and j, respectively, g_i is the statistical weight of level i, L denotes multipole designation which includes electric dipole, quadruple, magnetic dipole and quadruple in our code, α is the fine-structure constant, ΔE is the transition energy between level i and j, and O_M^L is the tensorial operator. The oscillator strength is connected with radiative rate in the following way:

$$f_{ij} = \frac{A_{ij}}{2\alpha^3(\Delta E)^2}. \tag{7}$$

The photoionization cross section from level i to j can be written as

$$\sigma_{ij}^{\mathrm{PI}} = 2\pi\alpha\frac{df}{dE}, \tag{8}$$

where df/dE is the differential oscillator strength and it can be obtained in a similar manner to the bound–bound transitions by

replacing one bound orbital in the final state with the free orbital of the ionized electron:

$$\frac{\mathrm{d}f}{\mathrm{d}E} = \frac{\Delta E(\alpha\Delta E)^{2L-2}}{g_i(2L+1)} \sum_{\kappa J_\mathrm{T}} \left|\left\langle \Psi_j, \kappa; J_T \parallel O^L \parallel \Psi_i \right\rangle\right|^2, \tag{9}$$

where κ is the relativistic quantum number of the free electron, J_T is the total angular momentum of the free electron coupled with the ionized upper bound state Ψ_j, g_i is the statistical weight of the initial state, ΔE is the energy difference between the initial and final states, and O^L is the multipole operator inducing the transition.

For electron impact excitation from level i to j, the cross section can be expressed in terms of the collision strength $\Omega_{ij}^{\mathrm{EIE}}$ as

$$\sigma_{ij}^{\mathrm{EIE}} = \frac{\pi}{k_0^2 g_i} \Omega_{ij}^{\mathrm{EIE}}, \tag{10}$$

where k_0 is the kinetic momentum of the incident electron and g_i is the statistical weight of the initial state. The collision strength can be expressed as

$$\Omega_{ij}^{\mathrm{EIE}} = 2\sum_{\kappa_i\kappa_j} \sum_{J_\mathrm{T}} \frac{1}{2J_\mathrm{T}+1} \left| \left\langle \Psi_j \kappa_j, J_\mathrm{T} M_\mathrm{T} \left| \sum_{m<n} \frac{1}{r_{mn}} \right| \Psi_i \kappa_i, J_\mathrm{T} M_\mathrm{T} \right\rangle \right|^2, \tag{11}$$

where κ_i and κ_j are the relativistic angular quantum numbers of the incident and scattered electrons, respectively, J_T is the total angular momentum of the target state coupled with the free electron and M_T is the projection of J_T.

The cross section of electron impact ionization can be obtained from that for electron impact excitation by replacing one bound orbital in the final state with the free orbital of the ejected electron and summing over its angular momentum. It can be written as

$$\sigma_{ij}^{\mathrm{EII}}(\varepsilon_0, \varepsilon) = \frac{1}{k_0^2 g_i} \Omega_{ij}^{\mathrm{EII}}, \tag{12}$$

where ε_0 and $k_0$are the energy and kinetic momentum of the incident electron and ε is the energy of the ejected electron. The collision strength of electron impact ionization can be expressed as

$$\Omega_{ij}^{\mathrm{EII}} = 2\sum_{\kappa_i\kappa_j\kappa_\mathrm{e}} \sum_{J_\mathrm{T}, M_\mathrm{T}} \frac{1}{2J_\mathrm{T}+1} \left| \left\langle \Psi_j \kappa_j, \kappa_e; J_T M_T \left| \sum_{m<n} \frac{1}{r_{mn}} \right| \Psi_i \kappa_i \right\rangle \right|^2, \tag{13}$$

where κ_e is the relativistic angular quantum number of the ejected electron.

The autoionization rate from level i to j is expressed as

$$A_{ij}^a = 2\sum_{\kappa} \left| \left\langle \Psi_j, \kappa; J_\mathrm{T} M_\mathrm{T} \left| \sum_{m<n} \frac{1}{r_{mn}} \right| \Psi_i \right\rangle \right|^2, \tag{14}$$

where κ is the relativistic angular quantum number of the ionized electron.

For some cases, two-electron processes such as direct double Auger and double photoionization are nontrivial and should be included in the rate equations. The atomic data of direct two-electron processes can be obtained by our recently developed code [33]. In this work, we do not give detailed description on the direct two-electron and multi-electron processes, yet their inclusion in the rate equations is straightforward.

2.2. Plasma screening effects module

The ions are embedded in the environment of plasmas, and therefore the atomic structure will be effected. If the plasma density is not very high, then we can deal with it in an approximate way. Three models are usually utilized to deal with the ionization potential depression (IPD) caused by the plasma screening effects, Debye–Hückel model, ion-sphere model and Stewart–Pyatt model [34,35].

In Debye–Hückel model, the largest radius of an electron which can still be bound is determined by the Debye radius. The IPD $\Delta\varphi_i$ of the ion i can be expressed as

$$\Delta\phi_i = z_i e^2 \sqrt{\frac{4\pi e^2 n_\mathrm{e}}{kT_\mathrm{e}}}, \tag{15}$$

where z_i is the charge of the ion i ($z_i = 1$ for neutral), n_e and T_e are the electron density and temperature, respectively.

For ion-sphere model, the electrons are assumed bound until they are close to a neighboring ion. Therefore the largest allowed radius is the average inter-ion distance. The IPD $\Delta\phi_i$ of ion i can be written as

$$\Delta\phi_i = \frac{3z_i e^2}{2R}, \tag{16}$$

where $R = ((3/4\pi z)^*/(n_e))^{1/3}$ (z^* is the average ionization) is the ion-sphere radius.

For Stewart–Pyatt model, the IPD is expressed as

$$\Delta\phi_i = \frac{\left[3(z^*+1)\frac{z_i e^2}{DkT}+1\right]^{2/3}}{2(z^*+1)} kT_\mathrm{e}, \tag{17}$$

where $D = \sqrt{kT_\mathrm{e}/4\pi n_\mathrm{e} e^2}$ is the Debye length. Once the IPD of all ion stages in the plasma are obtained, the outermost bound orbital nl is determined for each ion stage. The configurations with the valence orbital above the outermost bound orbital nl are considered as ionized and the levels belonging to those configurations should be removed from the rate equation.

For dense plasmas, i.e., near or above solid density, the plasma screening effects can affect the basic atomic data [36–38]. Li et al. [37] proposed a method of using a self-consistent potential to account for the plasma screening effects on the atomic data. Considering an ion with nuclear charge Z, bound electrons N_b and radius R embedded in a hot dense plasma with temperature T_e and free electron density n_e, we find that in an ion sphere the average potential produced by the free electrons for the ith bound electron is expressed as

$$V(r_i) = 4\pi\left[\frac{1}{r_i}\int_0^{r_i} + \int_{r_i}^{R}\right] r_1 \rho_\mathrm{f}(r_1)\mathrm{d}r_1, \tag{18}$$

where $\rho_\mathrm{f}(r)$ is the free electron density distribution in the ion-sphere. $\rho_\mathrm{f}(r)$ is assumed to follow the Fermi-Dirac distribution of the local free electron gas in the plane wave momentum k space and can be defined as

$$\rho_\mathrm{f}(r) = \frac{1}{\pi^2}\int_{k_0(r)}^{\infty} \frac{k^2\mathrm{d}k}{e^{\left[\sqrt{k^2c^2+c^4}-c^2-V(r)-\mu\right]/T}+1}, \tag{19}$$

where $k_0(r) = [2V(r)c^2 + V(r)^2]^{1/2}$and μ is the chemical potential. The chemical potential is determined by the neutrality condition

$$4\pi \int_0^R r^2 \rho_f(r) \mathrm{d}r = Z - N_b. \tag{20}$$

If the plasma screening effect is so strong that we must take its effect on the basic atomic data such as energy levels and various cross sections into account, then we utilize the method of self-consistent potential to obtain all required atomic data.

2.3. Rates module

After the atomic data are generated, we can determine the rates. The rates of the corresponding inverse processes can be obtained by the principle of detailed balance.

For microscopic atomic processes due to photons, the rate due to photo-excitation and photoionization from level i to j can be obtained from the corresponding cross section. For photo-excitation, this reads

$$B_{ij} = \int_0^\infty \frac{8\pi\nu^2}{c^2} f_\nu \sigma_{ij}^{\mathrm{PE}}(\nu) \mathrm{d}\nu, \tag{21}$$

where ν is the photon frequency, f_ν is the photon distribution function of the radiation field, c is the velocity of photons in vacuum, $\sigma_{ij}^{\mathrm{PE}}(\nu)$ is the photo-excitation cross section at the photon frequency ν. For a bound–bound transition, $\sigma_{ij}^{\mathrm{PE}}(\nu)$ can be expressed in terms of oscillator strengths f_{ij} as

$$\sigma_{ij}^{\mathrm{PE}}(\nu) = \frac{\pi h e^2}{m_e c} f_{ij} S(\nu), \tag{22}$$

where h is the Planck constant, m_e is the electron mass, $S(\nu)$ is the line profile that is, in general, a Voigt profile with natural lifetime broadening, Doppler and electron impact broadening widths taken into account [5]. For a wide-band radiation field such as blackbody radiation with a Planck distribution and very narrow line width, the integration of expression in B_{ij} can be approximated by

$$B_{ij} = \frac{8\pi\nu^2}{c^2} f_\nu \frac{\pi h e^2}{m_e c} f_{ij}. \tag{23}$$

For narrow-band radiation field such as X-ray free-electron lasers of the Linac Coherent Light Source (LCLS) [39], one has to integrate the contributions from the radiation field, as part of the line profile may be outside the photon distribution function. The radiative decay rate is the sum of the photo-deexcitation and spontaneous radiative decay rate

$$B_{ji} = g_i B_{ij}/g_j + A_{ji}. \tag{24}$$

For the photoionization process, the expression of the rate from level i to j is similar to that of photo-excitation

$$C_{ij} = \int_{\Delta E/h}^\infty \frac{8\pi\nu^2}{c^2} f_\nu \sigma_{ij}^{\mathrm{PI}} \mathrm{d}\nu, \tag{25}$$

where ΔE is the energy difference between levels i and j. The rate of the corresponding inverse process, radiative recombination, can be expressed as

$$C_{ji} = n_e \int_0^\infty \nu f(\nu)(1+f_\nu)\sigma_{ji}^r \mathrm{d}\nu, \tag{26}$$

where n_e is the electron density, σ_{ji}^r is the cross section of radiative recombination, v is the velocity of free electrons and $f(v)$ is the electron distribution function, which is generally assumed to be a Maxwellian distribution. According to the principle of detailed balance, one can obtain the relations between the cross section of photoionization and radiative recombination:

$$\sigma_{ji}^r = \frac{g_i}{g_j}\left(\frac{h\nu}{m_e \nu c}\right)^2 \sigma_{ij}^{\mathrm{PI}}. \tag{27}$$

The rate of electron impact excitation D_{ij} from level i to j can be written as

$$D_{ij} = n_e \int_{\sqrt{2\Delta E/m_e}}^\infty \nu f(\nu) \sigma_{ij}^{\mathrm{EIE}} \mathrm{d}\nu, \tag{28}$$

where ΔE is the energy difference between levels i and j, $\sigma_{ij}^{\mathrm{EIE}}$ is the cross section of electron impact excitation. According to the principle of detailed balance, the de-excitation rate D_{ji} can be obtained by

$$D_{ji} = \frac{g_i}{g_j} e^{\frac{\Delta E}{kT_e}} D_{ij}, \tag{29}$$

where T_e is the electron temperature.

The rate of electron impact ionization from level i to j can be expressed as

$$E_{ij} = n_e \int_{\sqrt{2\Delta E/m_e}}^\infty \nu f(\nu) \sigma_{ij}^{\mathrm{EII}} \mathrm{d}\nu, \tag{30}$$

where ΔE is the energy difference between levels i and j, and $\sigma_{ij}^{\mathrm{EII}}$ is the electron impact ionization cross section. According to the principle of detailed balance, the rate of three body recombination can be obtained by the following relation

$$E_{ji} = n_e \frac{1}{2} \frac{g_i}{g_j} \left(\frac{h^2}{2\pi m_e k T_e}\right)^{3/2} e^{\Delta E/kT_e} E_{ij}. \tag{31}$$

The autoionization rate A_{ij}^a from level i to level j has been obtained in the previous section

$$F_{ij} = A_{ij}^a. \tag{32}$$

According to the principle of detailed balance, the rate of dielectronic capture F_{ji} can be obtained by

$$F_{ji} = n_e \frac{1}{2} \frac{g_i}{g_j} \left(\frac{h^2}{2\pi m_e k T_e}\right)^{3/2} e^{-\Delta E/kT_e} A_{ij}^a, \tag{33}$$

where ΔE is the energy difference between levels i and j.

To construct a DCA method, the level-to-level rates obtained from above relativistic calculations are transformed to configuration-to-configuration rates by summing all final levels belonging to the final configuration and averaging over all initial levels belonging to the initial configuration. In this way, the accuracy of atomic data can be maintained as in the DLA formalism. If we want to keep detailed structure of the radiative properties, we construct a hybrid DLA/DCA method which employs a DLA formalism for the detailed structure and a DCA method for the smoothed background.

2.4. Collisional-radiative module

Combining all rates derived in the previous section, we set up a complete time-dependent rate equation (TDRE) which couples all levels (or configurations) in the plasmas

$$\frac{dn_i}{dt}=\sum_{j\neq i}^{N_L} n_j\left(B_{ji}+C_{ji}+D_{ji}+E_{ji}+F_{ji}\right)-n_i\sum_{j\neq i}^{N_L}\left(B_{ij}+C_{ij}+D_{ij}+E_{ij}+F_{ij}\right). \tag{34}$$

To solve this TDRE, additional constraint must be introduced to ensure population conservation

$$\sum_{i=1}^{N_L} n_i = N_{\text{ion}}, \tag{35}$$

and charge neutrality in the plasma

$$\sum_{i=1}^{N_L} z_i n_i = N_e, \tag{36}$$

where z_i is the ionization degree associated with level i, N_e is the population number of the electrons and N_{ion} is the population number of atoms and ions. The most pronounced characteristic is that the rates involved in the rate equation can differ by orders of magnitude and therefore it is a stiff problem. Therefore, we use a fourth Runge–Kutta method to solve the TDRE.

For plasmas in a steady state case, the rate equations are reduced to $dn_i/dt = 0$. A Gaussian elimination method is used to solve the set of linear equations. For the problems of large-scale rate equations, a parallel procedure is developed by calling the ScaLAPACK library [40], which is a library with subroutines for solving the most common problems in numerical linear algebra.

2.5. Radiative properties module

After solving the rate equation, one obtains the level populations that can be used to calculate the radiative properties of plasmas from the same set of atomic data. The emissivity $j(h\nu)$ at photon energy $h\nu$ contains contributions from bound–bound, free–bound and free–free processes

$$j(h\nu) = j_{\text{bb}}(h\nu)+j_{\text{fb}}(h\nu)+j_{\text{ff}}(h\nu). \tag{37}$$

The bound–bound contribution can be expressed as

$$j_{\text{bb}}(h\nu) = \sum_{j>i} n_j h\nu A_{ji} S(h\nu), \tag{38}$$

where n_j is the population of the upper level of the transition $j \to i$, A_{ji} and $S(h\nu)$ are the radiative transition probability and line profile of the transition $j \to i$, respectively.

The free–bound contribution can be written as

$$j_{\text{fb}}(h\nu) = \sum_{j,i} n_e n_j h\nu \frac{h\nu-\Delta E}{kT_e}\sqrt{\frac{16}{(2\pi m_e kT_e)}}\sigma_{ji}^{r} e^{-(h\nu-\Delta E)/kT_e}, \tag{39}$$

where n_e and T_e are the electron density and electron temperature, respectively, ΔE is the energy difference between levels i and j, and σ_{ji}^{r} is the cross section of radiative recombination.

The free–free contribution is

$$j_{\text{ff}}(h\nu) = \frac{2\sqrt{2}}{\sqrt{3\pi}}\alpha\sigma_T c n_e \frac{m_e c^2}{kT_e} g_{\text{ff}} e^{-h\nu/kT_e}\sum_{i=0}^{Z} N_i z_i^2, \tag{40}$$

where α is the fine structure constant, σ_T is the Thomson scattering cross section, g_{ff} is the Gaunt factor, Z is the nuclear charge, N_i is the population number of ion i and z_i is the effective nuclear charge of ion i.

A similar formula is employed for the radiative opacity and the details can be found elsewhere [41,42]. No additional description will be given here.

3. Results and discussions

As the theoretical methods of DCA and hybrid DLA/DCA models are similar to that of DLA and we therefore restrict the illustrative examples to two cases obtained using the DLA formalism. One is a steady state case for carbon plasmas and the other is a time-dependent case for the relaxation process that occurs for K-shell excited argon. For these two cases, the rates connecting ionization stages from H-like to Mg-like ions are used to set up the rate equations. In our calculations, the levels belonging to configurations from H-like to Mg-like ions are listed in Table 1 for the DLA calculation. The configurations include the ground, singly and doubly excited states with the maximum principal quantum number n up to 8 or 9. The guide line of such a choice of configurations is to ensure the convergence of results.

3.1. Steady state case: carbon

Carbon is one of the most important elements under investigation, since it is widely used in ICF [43] and international thermonuclear experimental reactor [44]. It has been selected as a test case by the NLTE workshops due to the relatively simple atomic structure [8]. To begin with, the convergence of the present calculation should be checked. Fig. 1 shows the charge state distribution (CSD) of a carbon plasma at an electron temperature of $T_e = 10$ eV and density of 10^{20} cm^{-3} without any radiation field, where $n_{\max}$ is the largest principal quantum number of the configurations included in the calculations. Although the discrepancies of the results for different $n_{\max}$ are small, the convergence behavior of the CSD can be seen in Fig. 1. With the increase of $n_{\max}$, the CSD gradually shifts to the lower ionization stages, with smaller shifts occurring as $n_{\max}$ increases. When $n_{\max}$ is set to 9, the CSD is almost the same as that for $n_{\max} = 7$. The most abundant ion stages are the Li-like and He-like carbon ions that have only 3 and 2 bound electrons, respectively. Further calculations with larger $n_{\max}$ show that the CSD has converged at $n_{\max} = 9$. For denser plasmas, the

Table 1
Configurations from H-like to Mg-like ions included for DLA calculation. $(n)^m$ means arbitrary distribution of m electrons in the shell with the principal quantum number n. $l = 0,1,2,\ldots,n-1$.

Ions	Configurations
H-like	nl $(n \le 9)$
He-like	$1s^2$, $nln'l'(n \le 3, n' \le 9)$
Li-like	$1s^2nl$ $(n \le 9)$; $1snln'l'$ $(n \le 3, n' \le 9)$
Be-like	$1s^2nln'l'$ $(n \le 3, n' \le 9)$; $1s(2)^2$ nl $(n \le 5)$
B-like	$1s^2(2)^2nl$ $(n \le 9)$; $1s^2(2)3lnl'$ $(n \le 5)$
C-like	$1s^2(2)^3nl$ $(n \le 9)$; $1s^2(2)^23lnl'$ $(n \le 5)$
N-like	$1s^2(2)^4nl$ $(n \le 8)$; $1s^2(2)^3lnl'$ $(n \le 5)$
O-like	$1s^2(2)^5nl$ $(n \le 8)$; $1s^2(2)^43lnl'$ $(n \le 5)$
F-like	$1s^2(2)^6nl$ $(n \le 8)$; $1s^2(2)^53lnl'$ $(n \le 5)$
Ne-like	$1s^2(2)^7nl$ $(n \le 8)$; $1s^2(2)^63lnl'$ $(n \le 5)$
Na-like	$1s^2(2)^8nl$ $(n \le 8)$; $1s^2(2)^73lnl'$ $(n \le 5)$
Mg-like	$1s^2(2)^8(3)nl$ $(n \le 8)$; $1s^2(2)^7(3)^2nl$ $(n \le 5)$

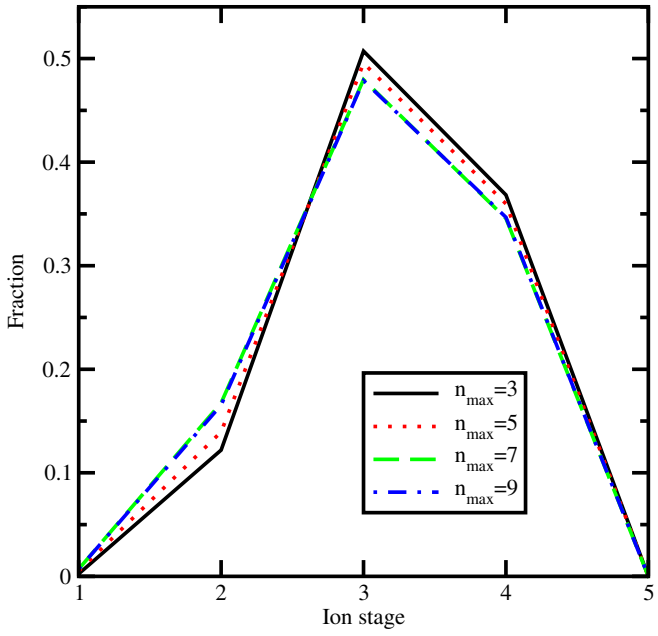

Fig. 1. The CSD of a carbon plasma at an electron temperature of 10 eV and density of 10^{20} cm^{-3}. n_{max} means the maximum principal quantum number included in the calculation.

maximum principal quantum number is truncated due to the effects of IPD and therefore it becomes sufficient to set n_{max} to 9. We also checked the convergence behavior of CSDs at smaller densities and found that the $n_{max} = 9$ is adequate for carbon plasmas at densities above 10^{15} cm^{-3}. With the increasing temperature larger values of n_{max} will be required.

After checking the convergence of the results, the population distributions of carbon plasmas over a wide range of electron density are calculated. In Fig. 2 we show in a solid line the average

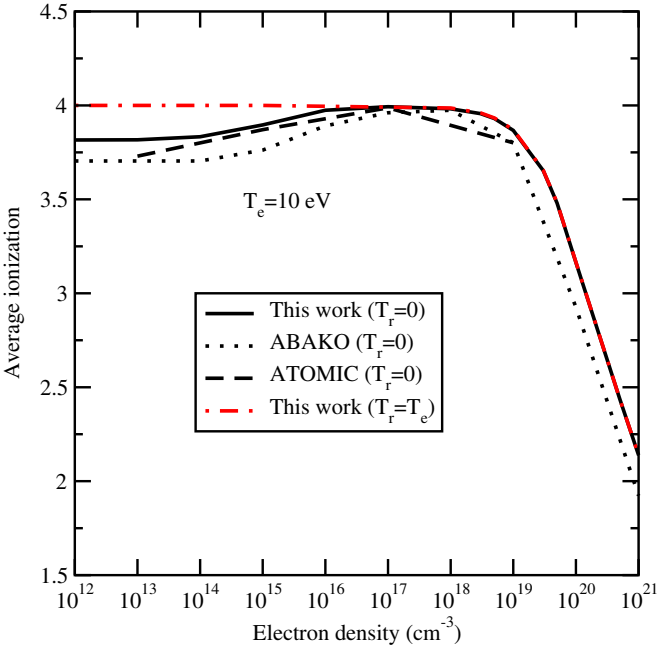

Fig. 2. Average ionization obtained by the present model as a function of electron density for carbon plasmas at electron temperature $T_e = 10$ eV and radiative temperature $T_r = 0$ and 10 eV. The results from ABAKO [21] and ATOMIC [24] at $T_r = 0$ are shown for comparison.

ionization of carbon plasmas for an electron temperature of $T_e = 10$ eV as a function of the electron density. For comparison, we also show the results obtained by Florido et al. using ABAKO code [21] and by Colgan et al. using the ATOMIC code [24] that are presented by dotted and dashed lines, respectively. The three results were obtained without radiation field, i.e., $T_r = 0$, meaning a complete NLTE condition. It can be seen that reasonably good agreement is found between the three theoretical results over the entire range of electron densities from 10^{12} to 10^{21} cm^{-3}, although evident discrepancies can be found at lower and higher electron density. At the electron density range of 10^{16}–10^{19} cm^{-3}, the average ionization is 4 indicating that the most abundant ion stage is the He-like C^{4+}, which is due to the high ionization potential of C^{4+}. At these plasma conditions, the population distribution and average ionization are insensitive to the different models and therefore the models using detailed calculation and analytical formula gave basically the same results. At density below 10^{16} cm^{-3} and above 10^{19} cm^{-3}, our predicted average ionization is larger than those of ABAKO. We suggest that such discrepancies should be due to the different models and different atomic data used. Yet all theoretical results predicted the same trend with the increase of electron density, the average ionization first increases with the increase of electron density and then decreases. Such a trend is consistent with the observation of the NLTE workshops [8].

Without radiation field, the steady state of NLTE plasmas is maintained by electron impact excitation and ionization which can be used as a check of the present calculation. To further check our model, we specify the average ionization stage for the same plasma condition but include a Planckian radiation field with the same temperature as the electron temperature, and the results are shown by the dot-dashed line in Fig. 2. This means that the radiation field and the electron are in thermodynamic equilibrium and therefore the NLTE models should give the same results as the Saha ionization equilibrium equation for the population distribution. We calculated the population distribution using the Saha equation and compared with that of NLTE computation, which verified this conclusion. Therefore, the DLA model is reliable. Below 10^{19} cm^{-3}, the result including a radiation field with the same temperature of the electron predicted a constant average ionization, which means that the coronal equilibrium condition is fulfilled for carbon plasmas below electron density of 10^{19} cm^{-3}. With increasing electron density the ionization and recombination are gradually dominated by the collisional processes due to the electrons. The radiation field of 10 eV can hardly affect the ionization balance and therefore the results of $T_r = T_e$ are the same as those of $T_r = 0$ at high densities.

At lower electron density, the population distribution deviates from LTE values, which can easily be seen in Fig. 3. As an example, Fig. 3 shows the ratio of NLTE ($T_r = 0$) to LTE ($T_r = T_e$) populations of energy levels belonging to configurations $1snl$ ($n = 2$–9) of C^{4+} at $T_e = 10$ eV. The electron density varies from 10^{12} to 10^{21} cm^{-3} and the horizontal axis represents level energies relative to the ground state of C^{4+}. From the inspection of Fig. 3, it is obvious that the population increasingly drops below the Boltzmann distribution (LTE) as the electron density is lowered. This deviation shows reproducible characteristic with the principal quantum number n. That is, for the same n, the levels with larger orbital angular momentum l deviate more strongly than those of lower l. With the increase of the electron density the population distribution becomes closer to the Boltzmann distribution. At the electron density above 10^{21} cm^{-3}, the ratio is nearly 1 and it shows that the population distribution is close to that of LTE. This means that the radiation field no longer has effects on the population distribution at higher electron density.

Autoionization (AI) and its inverse process dielectronic capture (DC) play an important role on the ionization balance and much

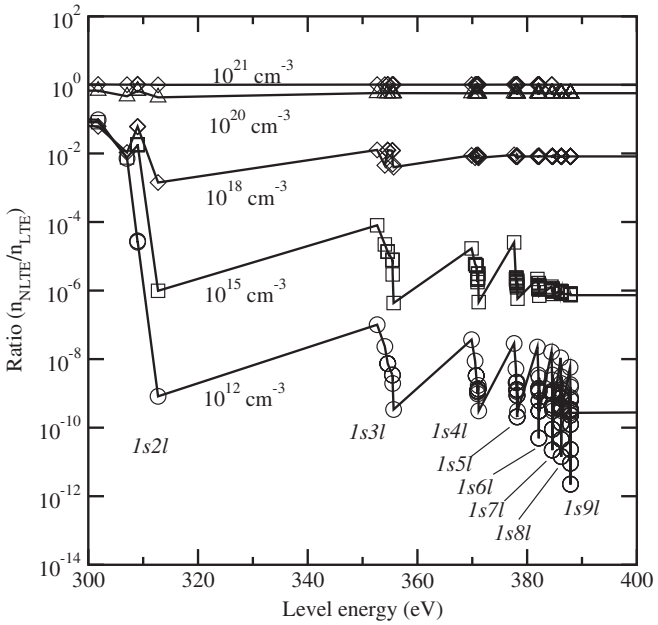

Fig. 3. The ratio of NLTE ($T_r = 0$) to LTE ($T_r = T_e$) populations of energy levels belonging to $1snl(n = 2–9)$ of C^{4+} at $T_e = 10$ eV and a variety of electron densities. The horizontal axis represents levels with energy relative to the ground state of C^{4+}.

research has been performed on the effects of AI/DC on population distributions [45,46]. Some NLTE codes calculate the AI rates with analytical formula and the accuracy of atomic data can be evaluated by using more accurate formalism [33,47]. The effects of AI/DC on the population distribution can be seen in Fig. 4, which shows the CSD of carbon plasmas at an electron temperature of 50 eV and a variety of electron density from 10^{12} to 10^{22} cm^{-3} without radiation field. The solid line with squares represents the result obtained by including AI/DC processes and the dashed line with circles by excluding AI/DC processes in our code. From inspection of Fig. 4, one finds that the average ionization without AI/DC processes is always lower than that of with AI/DC processes. The effects of AI/DC processes on the average ionization are not the same over the entire electron density range with the largest effects occurring at an electron density near 10^{21} cm^{-3}. With a further increase of electron density from 10^{21} to 10^{22} cm^{-3}, the results obtained by including and excluding AI/DC processes are closer and closer, converging to roughly the same value. Such a conclusion is consistent with the common knowledge that for high density plasmas the three-body recombination dominates the DC process so that inclusion of AI/DC processes gives roughly the same result as that of without AI/DC.

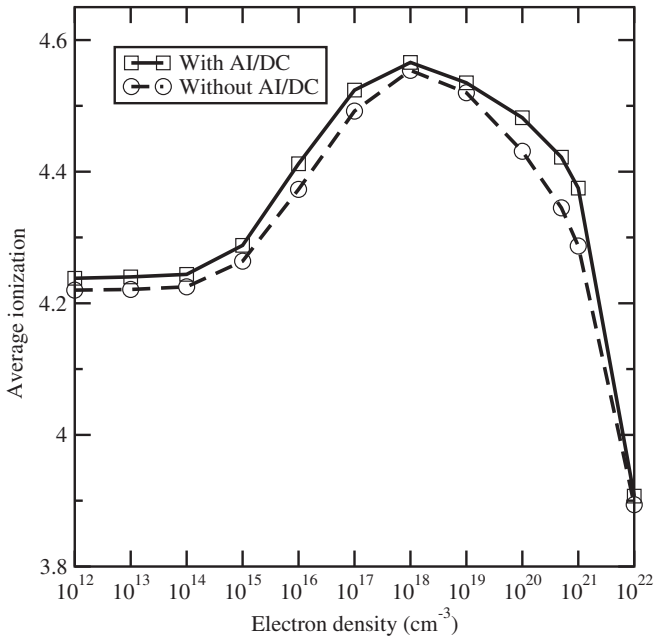

Fig. 4. Average ionization of carbon plasmas as a function of electron density at an electron temperature of 50 eV. The dashed line with circles represents the results obtained by excluding AI/DC processes.

For plasmas at high densities, the atomic structure and cross sections can be affected by the plasma environment [37,38]. One such effect is the IPD, a consequence of which is that the number of bound levels is no longer infinite. In principle, the IPD should be calculated by solving the Dirac equation of atomic structure with the plasma screening potential. For illustrative purposes we use the analytical Stewart–Pyatt model to implement the IPD [34]. Table 2 shows the IPD of carbon ions at an electron density of 10^{21} cm^{-3} and temperature of 50 eV. For each ion stage, the outermost valence orbital *nl* which is still bound is also listed. In practical calculations, the configurations with the valence shell higher than *nl* are considered ionized and the levels belonging to those configurations should be removed from the rate equations. From Table 2, one can see that plasma screening effects play a role on ionization potential. For example, the ionization potential of C^{4+} is lowered by 4.33 eV and the outermost bound orbital is 8*k*, which means orbitals above 8*k* are already free. For neutral C, the outermost bound orbital is 5*p* indicating that the plasma screening effects play a more important role on lower ionization stages. The total number of levels in the rate equation is greatly reduced due to IPD and the population distributions are consequently affected. The IPD effects on population distributions can be seen in Fig. 5, where the CSD of a carbon plasma at 50 eV and 10^{21} cm^{-3} is shown. The solid line with squares represents the result when including IPD effects and the dashed line with circles when excluding IPD effects. With the IPD effects being taken into account, the fraction of H-like C^{5+} is increased while that of Li-like C^{3+} is decreased, resulting in a higher average ionization.

After the population distributions are obtained, the radiative properties can be calculated. Fig. 6 shows the emission spectra of carbon plasmas at an electron temperature of 50 eV and electron density of (a) 10^{20} and (b) 10^{21} cm^{-3}. The emission lines of Heα, Heβ, Lyα and Lyβ are marked and the 1*s* ionization thresholds of C^{3+}, C^{4+} and C^{5+} are represented by arrows in panel (b). The structures in the emissivity below photon energy of 150 eV is contributed by the valence electron emission and those above photon energy of 200 eV are contributed by the inner-shell emission. Due to IPD, some levels with higher principal quantum number are merged in the continuum and therefore some emission lines in Fig. 6(b) have disappeared. The distinct character in the photon energy region of 350–400 eV of Fig. 6 is caused by the

Table 2
IPD and the outermost bound orbital *nl* of carbon ion stages at an electron density of 10^{21} cm^{-3} and an electron temperature of 50 eV.

Ions	IPD (eV)	*nl*
C	0.87	5*p*
C^{+}	1.73	6*h*
C^{2+}	2.60	7*p*
C^{3+}	3.46	7*p*
C^{4+}	4.33	8*k*
C^{5+}	5.20	9*l*

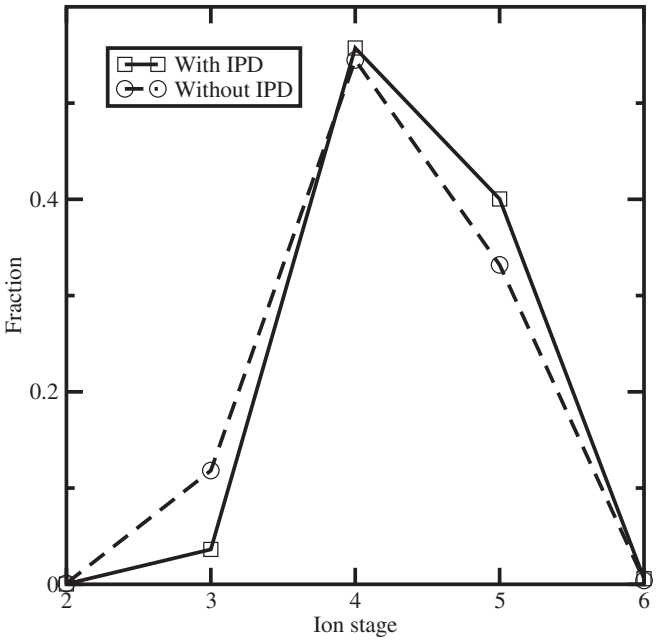

Fig. 5. CSD of a carbon plasma at an electron temperature of 50 eV and electron density of 10^{21} cm^{-3}. The dashed line with circles represents the results obtained by excluding the IPD effects.

different population distribution at the respective plasma condition. At higher electron density, the CSD favors lower ionization stages and more population is distributed into the excited states. As a result, the free-bound emission at 10^{21} cm^{-3} is more intense than that at 10^{20} cm^{-3}.

3.2. Time-dependent case: argon

In many cases, the steady state assumption does not hold and therefore one has to apply the TDRE approach to investigate the evolution of populations [48]. One such example is the interaction of X-ray free electron lasers such as LCLS [39,49] with atoms, molecules and clusters, where TDRE is widely employed to investigate the evolution dynamics of populations [28,50–52]. Here we consider the relaxation process of Ne-like argon after selective K-shell photoexcitation that can be achieved using X-ray free electron lasers such as LCLS and which is a test case in NLTE workshop [53]. It is assumed that at time $t = 0$ all population is in the $1s2s^22p^63p$

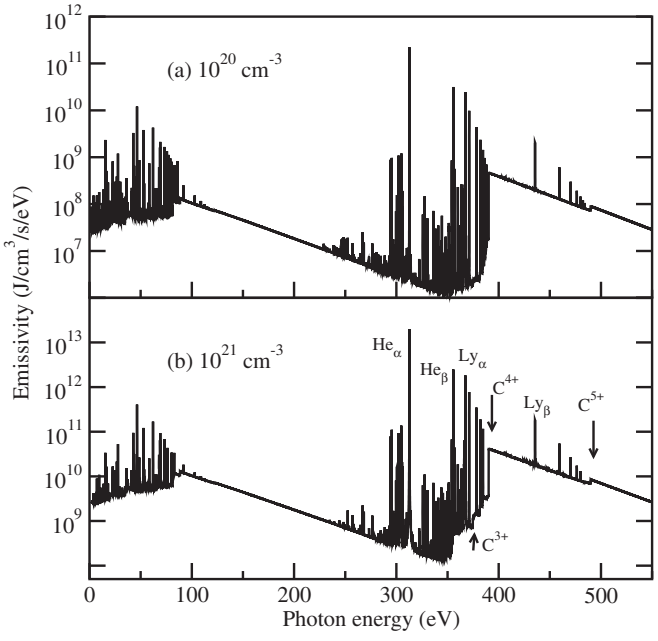

Fig. 6. The emissivity of carbon plasmas at $T_e = 50$ eV and electron density of (a) 10^{20} and (b) 10^{21} cm^{-3}. The locations of 1s ionization thresholds of C^{3+}, C^{4+} and C^{5+} are denoted by arrows.

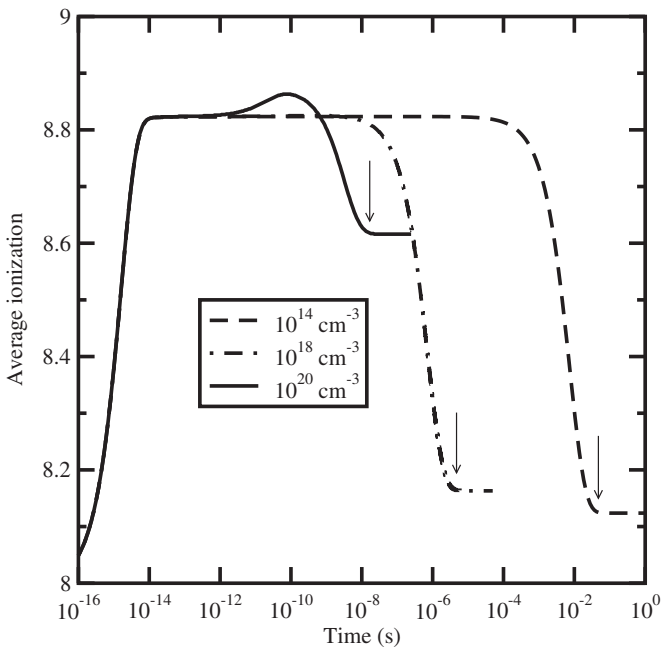

Fig. 7. Evolution of average ionization of argon plasma at an electron temperature of 50 eV and densities of 10^{14} cm^{-3} (dashed), 10^{18} cm^{-3} (dot-dashed) and 10^{20} cm^{-3} (solid). The arrows represent the time at which the plasma reaches steady state.

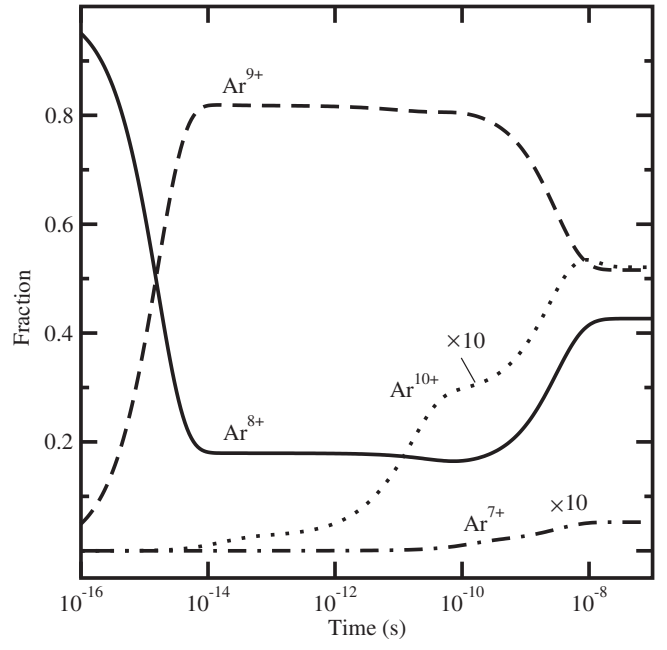

Fig. 8. Evolution of fractions of Ar^{7+}-Ar^{10+} at the temperature of 50 eV and density of 10^{20} cm^{-3}. The fractions of Ar^{7+} and Ar^{10+} are multiplied by a factor of 10 for illustrative purposes.

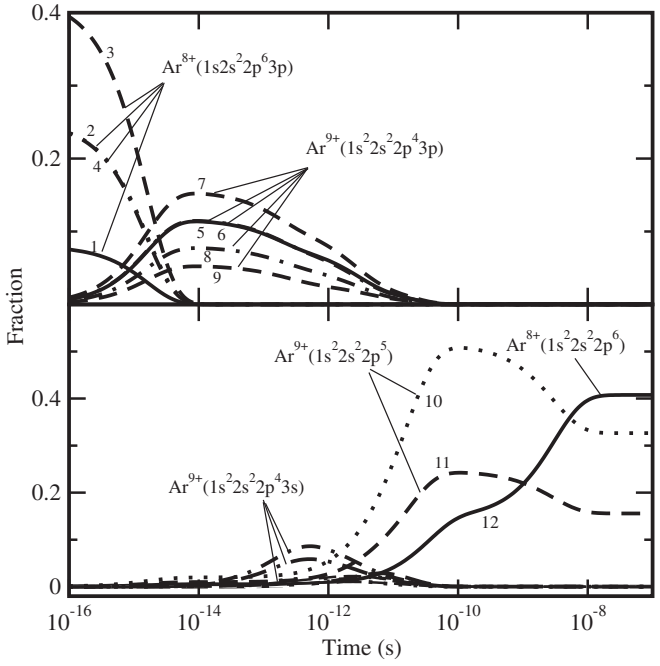

Fig. 9. Evolution of fractions for the most populated levels belonging to Ar^{8+} and Ar^{9+}. See Table 3 for the definition of labels 1–12.

configuration of Ar^{8+}. The electron temperature is chosen to be 50 eV and the initial populations are distributed amongst the four fine-structure levels of $1s2s^22p^63p$ according to their respective statistical weights. No radiation field is included in the calculation.

Fig. 7 shows the evolution of the average ionization of the argon plasma at electron densities of 10^{14}, 10^{18} and 10^{20} cm^{-3}, respectively, and the arrows represent the time points when the plasma reaches steady state at the respective density. At all electron densities, the average ionization increases rapidly at an earlier time of 10^{-16}–10^{-14} s and then keeps approximately constant for a time interval and then decreases rapidly. The evolution dynamics of the average ionization is irrelevant to the electron density from $t = 0$ to $t = 10^{-12}$ s. At this time duration, the evolution dynamics is predominantly due to the AI processes. As AI rates do not vary with time and hence the evolution is the same for all electron densities.

Table 3
Energy levels belonging to configurations of $1s^22s^22p^6$ and $1s2s^22p^63p$ of Ar^{8+}, $1s^22s^2p^5$ and $1s^22s^22p^43p$ of Ar^{9+}. In the designation of levels, full relativistic subshells have been omitted for simplicity.

Configuration	Level	No.
$1s^22s^22p^63p$	$(1s_{1/2}3p_{1/2})_0$	1
	$(1s_{1/2}3p_{1/2})_1$	2
	$(1s_{1/2}3p_{3/2})_2$	3
	$(1s_{1/2}3p_{3/2})_1$	4
$1s^22s^22p^43p$	$\left(\left(2p_{1/2}2p_{3/2}^3\right)_2 3p_{1/2}\right)_{5/2}$	5
	$\left(\left(2p_{1/2}2p_{3/2}^3\right)_2 3p_{3/2}\right)_{7/2}$	6
	$\left(\left(2p_{1/2}2p_{3/2}^3\right)_2 3p_{3/2}\right)_{3/2}$	7
	$\left(\left(2p_{1/2}2p_{3/2}^3\right)_2 3p_{3/2}\right)_{5/2}$	8
	$\left(\left(2p_{1/2}2p_{3/2}^3\right)_2 3p_{1/2}\right)_{3/2}$	9
$1s^22s^22p^5$	$\left(2p_{3/2}^3\right)_{3/2}(2p_{1/2})_{1/2}$	10
		11
$1s^22s^22p^6$	$(2s^22p^6)_0$	12

Table 4
Auger rates of the fine structure levels belonging to $1s2s^22p^63p \rightarrow 1s^22s^22p^43p + e$. Only rates larger than 5×10^{13} s^{-1} are given and X(Y) means $X \times 10^Y$.

Initial level	Final level	Rate (s^{-1})
$(1s_{1/2}3p_{1/2})_0$	$\left(\left(2p_{1/2}2p_{3/2}^3\right)_2 3p_{1/2}\right)_{5/2}$	1.86(14)
	$\left(\left(2p_{1/2}2p_{3/2}^3\right)_2 3p_{3/2}\right)_{3/2}$	5.31(13)
$(1s_{1/2}3p_{1/2})_1$	$\left(\left(2p_{1/2}2p_{3/2}^3\right)_2 3p_{1/2}\right)_{3/2}$	6.26(13)
	$\left(\left(2p_{1/2}2p_{3/2}^3\right)_2 3p_{1/2}\right)_{5/2}$	1.48(14)
	$\left(\left(2p_{1/2}2p_{3/2}^3\right)_2 3p_{3/2}\right)_{3/2}$	5.14(13)
$(1s_{1/2}3p_{3/2})_2$	$\left(\left(2p_{1/2}2p_{3/2}^3\right)_2 3p_{1/2}\right)_{3/2}$	5.25(13)
	$\left(\left(2p_{1/2}2p_{3/2}^3\right)_2 3p_{3/2}\right)_{7/2}$	1.45(14)
$(1s_{1/2}3p_{3/2})_1$	$\left(\left(2p_{1/2}2p_{3/2}^3\right)_2 3p_{3/2}\right)_{5/2}$	9.34(13)
	$\left(\left(2p_{1/2}2p_{3/2}^3\right)_2 3p_{1/2}\right)_{5/2}$	5.35(13)
	$\left(\left(2p_{1/2}2p_{3/2}^3\right)_2 3p_{3/2}\right)_{7/2}$	1.12(14)
	$\left(\left(2p_{1/2}2p_{3/2}^3\right)_2 3p_{3/2}\right)_{5/2}$	7.94(13)

With the increasing time different evolution trends are found at different electron densities. The evolution of the average ionization remains constant for longer time as the electron density lowered. The particular time points with a constant average ionization are $\sim 10^{-4}$, $\sim 10^{-8}$ and $\sim 10^{-10}$ s, for electron densities of 10^{14}, 10^{18} and 10^{20} cm^{-3}, respectively. After this time the average ionization decreases rapidly and finally reaches steady state. One can find that it takes a much longer time to reach a steady state for the plasma at 10^{14} cm^{-3} than at 10^{20} cm^{-3}. Such a trend is understandable, as with the increase of the electron density the electrons interact much more frequently with the ions and therefore the system can more rapidly arrive at a steady state. In the following, we take the plasma at 10^{20} cm^{-3} as an example to investigate the evolution dynamics of the different ion stages and populations of the detailed levels.

Table 5
Electron impact de-excitation rates of $1s^22s^22p^43p + e \rightarrow 1s^22s^22p^43s + e$ for Ar^{9+}. Only the rates larger than 1×10^{12} s^{-1} are given. X(Y) means $X \times 10^Y$.

Initial level	Final level	Rate (s^{-1})
$\left(\left(2p_{3/2}^2\right)_2 3p_{3/2}\right)_{5/2}$	$\left(\left(2p_{3/2}^2\right)_2 3s_{1/2}\right)_{5/2}$	1.69(12)
$\left(\left(2p_{3/2}^2\right)_2 3p_{3/2}\right)_{7/2}$	$\left(\left(2p_{3/2}^2\right)_2 3s_{1/2}\right)_{5/2}$	1.96(12)
$\left(\left(2p_{3/2}^2\right)_2 3p_{1/2}\right)_{5/2}$	$\left(\left(2p_{1/2}2p_{3/2}^3\right)_1 3s_{1/2}\right)_{3/2}$	1.66(12)
$(3p_{1/2})_{1/2}$	$\left(\left(2p_{1/2}2p_{3/2}^3\right)_1 3s_{1/2}\right)_{1/2}$	1.70(12)
$\left(\left(2p_{1/2}2p_{3/2}^3\right)_1 3p_{3/2}\right)_{5/2}$	$\left(\left(2p_{1/2}2p_{3/2}^3\right)_1 3s_{1/2}\right)_{3/2}$	1.83(12)
$(3p_{3/2})_{3/2}$	$\left(\left(2p_{1/2}2p_{3/2}^3\right)_1 3s_{1/2}\right)_{1/2}$	1.22(12)
$\left(\left(2p_{1/2}2p_{3/2}^3\right)_2 3p_{3/2}\right)_{7/2}$	$\left(\left(2p_{1/2}2p_{3/2}^3\right)_2 3s_{1/2}\right)_{5/2}$	2.01(12)
$\left(\left(2p_{1/2}2p_{3/2}^3\right)_2 3p_{3/2}\right)_{5/2}$	$\left(\left(2p_{1/2}2p_{3/2}^3\right)_2 3s_{1/2}\right)_{5/2}$	1.71(12)
$\left(\left(2p_{1/2}2p_{3/2}^3\right)_2 3p_{3/2}\right)_{5/2}$	$\left(\left(2p_{1/2}2p_{3/2}^3\right)_1 3s_{1/2}\right)_{3/2}$	1.75(12)
$\left(\left(2p_{1/2}2p_{3/2}^3\right)_2 3p_{3/2}\right)_{3/2}$	$\left(\left(2p_{1/2}2p_{3/2}^3\right)_1 3s_{1/2}\right)_{3/2}$	1.85(12)
$\left(\left(2p_{3/2}^2\right)_0 3p_{3/2}\right)_{3/2}$	$\left(\left(2p_{3/2}^2\right)_0 3s_{1/2}\right)_{1/2}$	1.93(12)

Table 6
Electron impact de-excitation rates of $1s^22s^22p^43p + e \rightarrow 1s^22s^22p^5 + e$ and radiative decay rates of $1s^22s^22p^43s \rightarrow 1s^22s^22p^5 + h\nu$ for Ar^{9+}. Only relatively large rates are listed.

Process	Initial level	Final level	Rate (s^{-1})
$1s^22s^22p^43p + e \rightarrow 1s^22s^22p^5 + e$	$\left(\left(2p_{1/2}2p^3_{3/2}\right)_2 3p_{3/2}\right)_{3/2}$	$(2p^3_{3/2})_{3/2}$	9.20(10)
	$\left(\left(2p^2_{3/2}\right)_0 3p_{3/2}\right)_{3/2}$	$(2p1/2)_{1/2}$	6.19(10)
	$(3p_{1/2})_{1/2}$	$(2p_{1/2})_{1/2}$	4.65(10)
$1s^22s^22p^43s \rightarrow 1s^22s^22p^5 + h\nu$	$\left(\left(2p_{1/2}2p^3_{3/2}\right)_1 3s_{1/2}\right)_{3/2}$	$\left(2p^3_{3/2}\right)_{3/2}$	3.02(11)
			1.49(11)
	$\left(\left(2p_{1/2}2p^3_{3/2}\right)_1 3s_{1/2}\right)_{1/2}$	$\left(2p^3_{3/2}\right)_{3/2}$	1.51(11)
	$\left(\left(2p_{1/2}2p^3_{3/2}\right)_2 3s_{1/2}\right)_{5/2}$	$\left(2p^3_{3/2}\right)_{3/2}$	
	$\left(\left(2p_{1/2}2p^3_{3/2}\right)_1 3s_{1/2}\right)_{1/2}$	$(2p^{1/2})_{1/2}$	2.32(11)
	$\left(\left(2p_{1/2}2p^3_{3/2}\right)_2 3s_{1/2}\right)_{3/2}$	$(2p_{1/2})_{1/2}$	1.48(11)

Fig. 8 shows the evolution of Ar^{7+}-Ar^{10+} at the density of 10^{20} cm^{-3}, where the fractions of Ar^{7+} and Ar^{10+} are multiplied by a factor of 10 for illustrative purposes. From an inspection of Fig. 8, one can find that Ar^{8+} and Ar^{9+} are the most abundant ionization stages in the plasma accounting for ~95%, and that Ar^{7+} and Ar^{10+} account for <5%. The evolution of different ionization stages shows different features. In the time interval of 10^{-16}–10^{-14} s, the fraction of Ar^{8+} decreases rapidly and the fraction of Ar^{9+} increases rapidly. In this time interval, the fractions of Ar^{7+} and Ar^{10+} are very small. This is the reason that the average ionization increases rapidly in this time interval, as discussed above with respect to Fig. 7. In the time interval from 10^{-14} to 10^{-10} s, the fractions of both Ar^{8+} and Ar^{9+} change little and consequently the average ionization changes little. During the interval from 10^{-12} to 10^{-10} s, the fraction of Ar^{10+} increases slowly to ~0.03 leading to a small increase of average ionization as shown in Fig. 7. In the interval from 10^{-10} to 10^{-8} s, the fraction of Ar^{8+} increases and that of Ar^{9+} decreases and consequently the average ionization decreases rapidly. From 10^{-8} s, Ar^{7+}–Ar^{10+} reach a steady state and as a result the average ionization reaches a constant value.

Fig. 9 shows the fraction of some of the most abundant levels belonging to Ar^{8+} and Ar^{9+}. For convenience, the fine-structure levels are labeled as 1–12 which are listed in Table 3. In the interval from 10^{-16} to 10^{-14} s, the populations of the four autoionization levels belonging to $1s2s^22p^63p$ of Ar^{8+} decrease rapidly and the populations of the levels belonging to $1s^22s^22p^43p$ of Ar^{9+} increase, which is caused by the autoionization of $1s2s^22p^63p \rightarrow 1s^22s^22p^43p + e$. To support this conclusion, Table 4 lists the autoionization rates of $1s2s^22p^63p \rightarrow 1s^22s^22p^43p + e$, where only the rates larger than 5×10^{13} s^{-1} are shown for simplicity. At the later time from 10^{-14} to 10^{-12} s, the populations of the levels belonging to $1s^22s^22p^43p$ of Ar^{9+} decrease and the populations of the levels belonging to $1s^22s^22p^43s$ of Ar^{9+} begin to increase. This is mainly cased by the electron impact de-excitation of $1s^22s^22p^43p + e \rightarrow 1s^22s^22p^43s + e$ as the corresponding rates are on the order of 10^{12} s^{-1} while the radiative transition rates are much smaller. Table 5 shows some important electron impact de-excitation channels. From 10^{-12} to 10^{-10} s, the populations of $1s^22s^22p^43p$ and $1s^22s^22p^43s$ of Ar^{9+} decrease and the populations of $1s^22s^22p^5$ of Ar^{9+} increase. This is mainly caused by the combined effects of the electron impact de-excitation of $1s^22s^22p^43p + e \rightarrow 1s^22s^22p^5 + e$ and radiative decay of $1s^22s^22p^43s \rightarrow 1s^22s^22p^5 + h\nu$ and the rates of the main channels are listed in Table 6. During the interval from 10^{-10} to 10^{-8} s, the populations of $1s^22s^22p^5$ of Ar^{9+} decrease and those of $1s^22s^22p^6$ of Ar^{8+} increase. The radiative recombination of $1s^22s^22p^5 + e \rightarrow 1s^22s^22p^6 + h\nu$ is the reason of this trend.

The results obtained by using DCA formalism can be found elsewhere [11]. The hybrid method for investigating the radiative opacity of LTE plasmas can be utilized to construct NLTE models [54]. The effects of direct double Auger and photoionization were discussed in the X-ray interaction with neon atoms in Ref. [28].

4. Conclusion

In conclusion, a NLTE code DLAYZ is presented for investigating the population kinetics and radiative properties of plasmas. The code is implemented with a DLA approach and can treat the steady state and time-dependent problems. The DLA formalism is extended to DCA and hybrid DLA/DCA approaches with the same atomic data by a configuration averaging method, which is very useful especially for high-Z plasmas. The complete set of atomic data between fine-structure levels including single photon and single electron processes are obtained by calculations using full relativistic quantum mechanics. The direct double electron processes such as double Auger and double photoionization can be included in the code. The plasma screening effects on the atomic structure and atomic processes can be taken into account. In the present illustrative examples, the plasma screening effects are described in terms of a lowering of the ionization potential by using analytical formula of Stewart–Pyatt model. For mid-Z or high-Z plasmas, the determination of the population distributions usually involves large-scale rate equations and therefore a parallelized method is developed for DLAYZ code. Two examples were given to show the main features.

Acknowledgment

This work was supported by the National Natural Science Foundation of China under Grants No. 11074306, 11204376, 11274382 and 11274383. Calculations are carried out at the Research Center of Supercomputing Application, NUDT.

References

[1] N.Y. Orlov, S.Y. Guskov, S.A. Pikuz, V.B. Rozanov, T.A. Shelkovenko, N.V. Zmitrenko, D.A. Hammer, Laser Part. Beams 25 (2007) 415.
[2] J. Bauche, C. Bauche-Arnoult, O. Peyrusse, J. Quant. Spectrosc. Radiat. Transfer 99 (2006) 55.
[3] J. Dai, D. Kang, Z. Zhao, Y. Wu, J. Yuan, Phys. Rev. Lett. 109 (2012) 175701.
[4] C.A. Iglesias, M.H. Chen, V. Sonnad, B.G. Wilson, J. Quant. Spectrosc. Radiat. Transfer 81 (2003) 227.
[5] C. Gao, J. Zeng, Phys. Rev. E 78 (2008) 046407.
[6] J. Zeng, J. Yuan, Phys. Rev. E 74 (2006) 025401(R).
[7] J. Zeng, J. Yuan, Phys. Rev. E 66 (2002) 016401.
[8] R.W. Lee, J.K. Nash, Yu Ralchenko, J. Quant. Spectrosc. Radiat. Transfer 58 (1997) 737;
C. Bowen, A. Decoster, C.J. Fontes, K.B. Fournier, O. Peyrusse, Yu.V. Ralchenko, J. Quant. Spectrosc. Radiat. Transfer 81 (2003) 71;
C. Bowen, R.W. Lee, Yu Ralchenko, J. Quant. Spectrosc. Radiat. Transfer 99 (2006) 102;

J.G. Rubiano, R. Flordo, C. Bowen, R.W. Lee, Yu Ralchenko, High Energy Density Phys. 3 (2007) 225;
C.J. Fontes, J. Abdallah Jr., C. Bowen, R.W. Lee, Yu. Ralchenko, High Energy Density Phys. 5 (2009) 15.
[9] C.J. Fontes, J. Colgan, H.L. Zhang, J. Abdallah Jr., J. Quant. Spectrosc. Radiat. Transfer 99 (2006) 175;
C.J. Fontes Jr., J. Abdallah, R.E.H. Clark, D.P. Kilcrease, J. Quant. Spectrosc. Radiat. Transfer 65 (2000) 223.
[10] J. Abdallah Jr., M.E. Sherrill, High Energy Density Phys. 4 (2008) 124.
[11] C. Gao, F. Jin, J. Zeng, J. Yuan, New J. Phys. 15 (2013) 015022.
[12] J. Yuan, Phys. Rev. E 66 (2002) 047401;
Y. Hou, F. Jin, J. Yuan, Phys. Plasma 13 (2006) 093301.
[13] Z.Q. Wu, G.X. Han, J. Yan, J.Q. Pang, J. Quant. Spectrosc. Radiat. Transfer 87 (2004) 367.
[14] V.G. Novikov, S.V. Zakharov, J. Quant. Spectrosc. Radiat. Transfer 81 (2003) 339.
[15] C.E. Starrett, D. Saumon, High Energy Density Phys. 8 (2012) 101.
[16] B. Wilson, V. Sonnad, P. Sterne, W. Isaacs, J. Quant. Spectrosc. Radiat. Transfer 99 (2006) 658.
[17] A. Bar-Shalom, J. Oreg, M. Klapisch, J. Quant. Spectrosc. Radiat. Transfer 58 (1997) 427.
[18] O. Peyrusse, J. Quant. Spectrosc. Radiat. Transfer 71 (2001) 571;
O. Peyrusse, C. Bauche-Arnoult, J. Bauche, J. Phys. B At. Mol. Opt. Phys. 38 (2005) L137;
O. Peyrusse, J. Phys. B At. Mol. Opt. Phys. 33 (2000) 4303.
[19] J. Bauche, C. Bauche-Arnoult, O. Peyrusse, A. Bachelier, K.B. Fournier, C. Chenais-Popovics, J.-C. Gauthier, J. Quant. Spectrosc. Radiat. Transfer 81 (2003) 47.
[20] H.K. Chung, M.H. Chen, W.L. Morgan, Y. Ralchenko, R.W. Lee, High Energy Density Phys. 1 (2005) 3.
[21] R. Florido, R. Rodríguez, J.M. Gil, J.G. Rubiano, P. Martel, E. Mínguez, R.C. Mancini, Phys. Rev. E 80 (2009) 056402.
[22] H.A. Scott, S.B. Hansen, High Energy Density Phys. 6 (2010) 39.
[23] C. Gao, J. Zeng, Phys. Scr. T 144 (2011) 014037.
[24] J. Colgan, C.J. Fontes, J. Abdallah Jr., High Energy Density Phys. 2 (2006) 90.
[25] A. Bar-Shalom, M. Klapisch, J. Oreg, J. Quant. Spectrosc. Radiat. Transfer 71 (2001) 169.
[26] J. Zeng, G. Zhao, J. Yuan, Chin. Phys. Lett. 22 (2005) 1972.
[27] M. Poirier, F. de Gaufridy de Dortan, J. Appl. Phys. 101 (2007) 063308;
M. Poirier, J. Phys. B At. Mol. Opt. Phys. 41 (2008) 025701.
[28] W. Xiang, C. Gao, Y. Fu, J. Zeng, J. Yuan, Phys. Rev. A 86 (2012) 061401(R).
[29] S. Mazevet, J. Abdallah, J. Phys. B At. Mol. Opt. Phys. 39 (2006) 3419.
[30] P. Beiersdorfer, M.J. May, J.H. Scofield, S.B. Hansen, High Energy Density Phys. 8 (2012) 271.
[31] S.B. Hansen, J. Bauche, C. Bauche-Arnoult, M.F. Gu, High Energy Density Phys. 3 (2007) 109.
[32] M.F. Gu, Can. J. Phys. 86 (2008) 675.
[33] J. Zeng, P. Liu, W. Xiang, J. Yuan, Phys. Rev. A 87 (2013) 033419.
[34] J.C. Stewart, K.D. Pyatt Jr., Astrophys. J. 144 (1966) 1203.
[35] D.J. Heading, J.S. Wark, G.R. Bennett, R.W. Lee, J. Quant. Spectrosc. Radiat. Transfer 54 (1995) 167. and references therein.
[36] C. Gao, J. Zeng, J. Yuan, High Energy Density Phys. 7 (2011) 54.
[37] Y. Li, J. Wu, Y. Hou, J. Yuan, J. Phys. B At. Mol. Opt. Phys. 41 (2008) 145002.
[38] Y. Li, J. Wu, Y. Hou, J. Yuan, J. Phys. B At. Mol. Opt. Phys. 42 (2009) 235701.
[39] P. Emma, et al., Nat. Photon. 4 (2010) 641.
[40] L.S. Blackford, et al., ScaLAPACK Users' Guide, Society for Industrial and Applied Mathematics, Philadelphia, PA, 1997.
[41] J. Zeng, J. Yuan, Phys. Rev. E 76 (2007) 026401.
[42] J. Zeng, J. Phys. B At. Mol. Opt. Phys. 41 (2008) 125702.
[43] J. Filevich, J. Grava, M. Purvis, M.C. Marconi, J.J. Rocca, J. Nilsen, J. Dunn, W.R. Johnson, Laser Part. Beams 25 (2007) 47.
[44] C.H. Skinner, G. Federeci, Phys. Scr. T 124 (2006) 18.
[45] J. Bauche, C. Bauche-Arnoult, O. Peyrusse, High Energy Density Phys. 5 (2009) 51.
[46] V.L. Jacobs, High Energy Density Phys. 5 (2009) 80.
[47] C. Gao, J. Zeng, Phys. Rev. A 82 (2010) 062515.
[48] R.W. Lee, J.T. Larsen, J. Quant. Spectrosc. Radiat. Transfer 56 (1996) 535.
[49] L. Young, et al., Nature (London) 466 (2010) 56.
[50] N. Rohringer, R. Santra, Phys. Rev. A 76 (2007) 033416.
[51] B. Rudek, et al., Nat. Photon. 6 (2012) 858.
[52] S. Son, R. Santra, Phys. Rev. A 85 (2012) 063415.
[53] http://nlte.nist.gov/.
[54] C. Gao, J. Zeng, F. Jin, J. Yuan, High Energy Density Phys. 9 (2013) 419.